



### Science Arts & Métiers (SAM)

is an open access repository that collects the work of Arts et Métiers Institute of Technology researchers and makes it freely available over the web where possible.

This is an author-deposited version published in: <https://sam.ensam.eu>  
Handle ID: [.http://hdl.handle.net/10985/20622](http://hdl.handle.net/10985/20622)

#### To cite this version :

Mehrez AGNAOU, Abdelaziz OMARI, Antonio RODRIGUEZ DE CASTRO, Azita AHMADI-SENICHAULT - Numerical investigation of Herschel–Bulkley fluid flows in 2D porous media: Yielding behaviour and tortuosity - Computers & Chemical Engineering - Vol. 133, p.106662 - 2020

Any correspondence concerning this service should be sent to the repository

Administrator : [scienceouverte@ensam.eu](mailto:scienceouverte@ensam.eu)



# Numerical investigation of Herschel–Bulkley fluid flows in 2D porous media: Yielding behaviour and tortuosity

Antonio Rodríguez de Castro<sup>a,\*</sup>, Mehrez Agnaou<sup>b</sup>, Azita Ahmadi-Sénichault<sup>c</sup>, Abdelaziz Omari<sup>d</sup>

<sup>a</sup>Arts et Metiers Institute of Technology, MSMP, HESAM Université, F-51006 Châlons-en-Champagne, France

<sup>b</sup>Department of Chemical Engineering, University of Waterloo, 200 University Avenue West Waterloo, N2L 3G1 ON, Canada

<sup>c</sup>Arts et Metiers Institute of Technology, Université de Bordeaux, CNRS, INRA, INP, HESAM Université, F-33405 Talence, France

<sup>d</sup>I2M, Bordeaux-INP, CNRS, Esplanade des Arts et Métiers, 33405 Talence Cedex, France

Hydraulic tortuosity is commonly used as an input to macroscopic flow models in porous media, accounting for the sinuosity of the streamlines. It is well known that hydraulic tortuosity does not depend on the applied pressure gradient for Newtonian creeping flows. Nevertheless, this is not necessarily the case for yield stress fluids flows, given the directional nature of both yielding and shear-thinning behaviour. This study aims at a breakthrough on the relationship between the hydraulic tortuosity and the level of yielding. To do so, the hydraulic tortuosity of the flow paths is evaluated in 2D porous media by means of direct numerical simulations and subsequently put in relation with the morphological information of the medium provided by pore-network modelling. Moreover, the effects of pore dimensions, spatial disorder and rheological parameters on yielding behaviour are examined. In most situations, the reported tortuosity values are lower than those obtained for Newtonian fluids.

## 1. Introduction

Along with the rheology of the considered fluid, transport phenomena within the porous media are fundamentally influenced by structural properties, such as pore size distribution, mean pore connectivity and average tortuosity (Habisreuther et al., 2009). Among them, tortuosity is used to describe the sinuosity and interconnectedness of the pore space as it affects transport processes (Clennel, 1997). This concept was originally introduced by Kozeny (1927) and Carman (1937), and is commonly defined as the ratio between the average length of the actual fluid flow path through the porous matrix,  $L_e$ , and the apparent length of the porous medium,  $L$ . However, a wide range of definitions exist in different fields of science and engineering (Duda et al., 2011), which have been previously analysed and compared in several publications (Dullien, 1992; Clennel, 1997; Valdés-Parada et al., 2011; Ghanbarian et al., 2013; Agnaou et al. 2017). Moreover, Agnaou et al. (2017) focused on the dependence of the tortuosity of the flow on the pore scale Reynolds number to predict the onset of different inertial regimes in non-creeping motion.

When modelling the relationship between pressure drop and flow rate, tortuosity is often defined as being the average elongation of a streamline in a porous medium, and is referred to as hydraulic tortuosity (Duda et al., 2011). The hydraulic tortuosity  $T = L_e/L$  is then used to account for the fact that the effective length of the fluid flow path within the porous medium  $L_e$  is greater than the apparent length  $L$  of the porous medium. Consequently,  $T$  has been commonly used as a significant input for predicting the hydraulic conductivity of a porous medium (Dullien, 1992; Vidal et al., 2009; Valdés-Parada et al., 2011; Ghanbarian et al., 2013). By assuming that the flow rate vs. pressure drop relationship during one-dimensional horizontal flow through a 2D porous medium sample of length  $L$  can be assimilated to that obtained in a bundle of rectangular channels having the same length  $L$ , infinite width, and  $N$  different aperture classes  $h_i$  ( $i = 1 \dots N$ ), the total flow rate  $Q$  per unit width is written as:

$$Q(\Delta P) = \sum_{i=1}^N n_i q(\Delta P, h_i) \quad (1)$$

where  $\Delta P$  is the pressure drop between the inlet and the outlet of the bundle,  $h_i$  is the representative pore aperture of the  $i$ th class of capillaries and  $n_i$  is the frequency of the  $i$ th class. In this equation, the  $(n_i, h_i)_i$  data correspond to the pore size distribution of the

\* Corresponding author.

E-mail address: antonio.rodriguezdecastro@ensam.eu (A. Rodríguez de Castro).

investigated medium, and  $q(\Delta P, h_i)$  is the individual flow rate per unit width in a rectangular channel of aperture  $h_i$ , under a pressure gradient  $\Delta P$ . In the case of creeping flow of a Newtonian fluid of dynamic viscosity  $\mu$ ,  $q(\Delta P, h_i)$  is given by Hele-Shaw's equation:

$$q(\Delta P, h_i) = \frac{h_i^3}{12\mu} \frac{\Delta P}{TL} \quad (2)$$

Other expressions of  $q(\Delta P, h_i)$  are available for the flow of non-Newtonian fluids, including yield stress fluids (Skelland, 1967; Chhabra and Richardson, 2008). It is worth noting that the use of Eqs. (1) and (2) to obtain flow rate vs. pressure drop relationship assumes that all channels have equal tortuosity value  $T$ . Therefore, if the specific hydraulic tortuosity of the streamlines is known for each pore class, the accuracy of the  $Q$  vs  $\Delta P$  predictions with the bundle-of-capillaries model is expected to be noticeably improved.

Another important issue concerns the determination of local pore velocity, shear rate and viscosity from easily measurable macroscopic Darcy's velocity  $u$ . By taking tortuosity into account, the average effective flow velocity  $V_p$  within a porous medium of porosity  $\varepsilon$ , expressed as  $V_p = (u/\varepsilon) \times T$  (Carman, 1937), can be determined. Consequently, assuming  $T = 1$  in a porous medium that is tortuous by nature leads to underestimation of  $V_p$ , which is not a trivial matter when dealing with non-Newtonian fluids with shear-rate-dependent viscosity. For example, if shear-thinning polymer solutions are considered, underestimation of  $V_p$  results, in turn, in underestimation of local shear rate and overestimation of local shear viscosity. Moreover, other effects of fluid-medium interactions on the adsorption, mechanical degradation and retention of macromolecules that are frequently encountered in the flow of such complex fluids are expected to be more impacted in the case of highly tortuous porous media, given that the residence time increases with  $T$ .

Different numerical approaches are currently available for determining tortuosity from the results of different experimental methods. In this respect, 3D images obtained by Nuclear Magnetic Resonance technique (NMR) were used by Habisreuther et al. (2009) to achieve numerical determination of structural tortuosity. Also, Laudone et al. (2015) presented an algorithm allowing the calculation of tortuosity in different types of porous media by using the mercury intrusion porosimetry results as input data. More recently, Pawlowski et al. (2018) derived hydraulic tortuosity from numerically simulated fluid pathways in the internal structure of a monolith reconstructed using 3D X-ray tomography images. In any case, attention must be paid to the differences between geometrical tortuosity and hydraulic tortuosity when analysing the results provided by these tortuosity characterization methods (Ghanbarian et al., 2013). Indeed, as emphasized by Clennel (1997), the paths taken by a fluid as it flows through the porous medium are not straight lines, or close tangents to the solid grains, but they are rather smooth curves tending to follow the axes of the flow channels. Also, as a result of viscous drag, fluid flow is more retarded at the channel walls than along the mean channel axes, so not all paths are equally intricate.

Previous works showed that, in the case of creeping Newtonian flow through a porous medium, the hydraulic tortuosity of the streamlines is independent of injection velocity (Sivanapillai et al., 2014; Ghanbarian et al., 2013; Agnaou et al., 2017; Zhang et al., 2019), and several relationships were proposed to estimate its value, as summarized by Ghanbarian et al. (2013). Whereas various definitions are only based on the actual length of the streamlines, others introduce a weighting factor such as the local velocity magnitude or flux which gives more importance to the streamlines with high velocity. Unlike in the case of Newtonian fluids, little attention has been paid to the evaluation of hydraulic tortuosity during flow of non-Newtonian fluids. In particular, the

available numerical studies addressing yield stress fluid flow in porous media are remarkably scarce (Chevalier and Talon, 2015; Malvault et al., 2017; Bao et al., 2017; Rodríguez de Castro and Agnaou, 2019; Kostenko and Talon, 2019; Rodríguez de Castro et al., 2020), due partly to the considerable computational resources required to perform direct numerical simulations of these complex flows (Saramito and Wachs, 2017).

Recently, Zhang et al. (2019) carried out 3D numerical simulations of the flow of non-yielding shear-thinning fluids obeying a Cross rheological law that contains an upper and a lower viscosity plateau through a rough-walled rock fracture, using an input geometry extracted from a digitalized microtomography image. In this work, the authors determined the hydraulic tortuosity of the flow from the detailed velocity field provided by the numerical simulations. They found that the hydraulic tortuosity of such a shear-thinning flow decreases with increasing flow rate within the creeping flow regime. In their analysis, they attributed this behaviour to the flow channelling effect observed when the local viscosity of the considered Cross fluids falls below the upper Newtonian plateau value in only a part of the fracture, i.e., in the largest pores where larger shear rates are generated. Also, Kostenko and Talon (2019) analyzed the fractal flow structures exhibited by yield stress fluids with constant plastic viscosity (Bingham fluids) in the presence of local heterogeneities by performing 2D Lattice Boltzmann simulations. These authors qualitatively observed that hydraulic tortuosity was higher in the presence of strong permeability heterogeneities. Such heterogeneities result in a considerable increase in the value of the local hydraulic tortuosity, as the flow is diverted towards the high-permeability regions of the medium.

The relationship between hydraulic tortuosity and injection velocity in the presence of a yield stress has still not been addressed in the literature, nor have the specific effects of pore body and throat size distributions and structural disorder been elucidated. In an attempt to fill this gap, the major objective of the present paper is to investigate the dependency of hydraulic tortuosity on the yielding degree of yield stress fluids obeying the Herschel-Bulkley law flowing through a porous medium. Moreover, the proportion of the fluid having yielded at different values of the Herschel-Bulkley number (which will be defined below) will also be characterized. In order to achieve these goals, a set of numerical simulations are performed by using 2D porous media with different microstructural characteristics. In these simulations, the fraction of the stagnant fluid and the tortuosity of the streamlines are calculated from the computed shear viscosity and velocity maps for different values of the Herschel-Bulkley number. To go further, the effects of Herschel-Bulkley parameters (i.e., yield stress, consistency and fluidity indexes) on the investigated relationships will be assessed by performing a second set of numerical experiments with different Herschel-Bulkley fluids through a given porous medium.

## 2. Numerical experiments

### 2.1. Microstructure of porous media under investigation

A subset of 2D micromodels presented by Mehmani and Tchelepi (2017a) was used in the current research (Fig. 1). This choice will allow us to assess the effect of disorder, grain sizes and polydispersity on the hydraulic tortuosity of the streamlines for the steady flow of Newtonian and yield stress fluids. In the particular case of the Berea 2D micromodel, the geometry was previously extracted by Boek and Venturoli (2010) based on a thin slice of a 3D Berea sandstone rock sample. Table 1 lists the main microstructural features, the permeability  $K$ , the porosity  $\varepsilon$  and the value of the hydraulic tortuosity of the flow paths followed by Newtonian fluids,  $T_N$ , for all the used micromodels.  $T_N$  was obtained from the results of direct numerical simulations as those presented in Section 2.2.

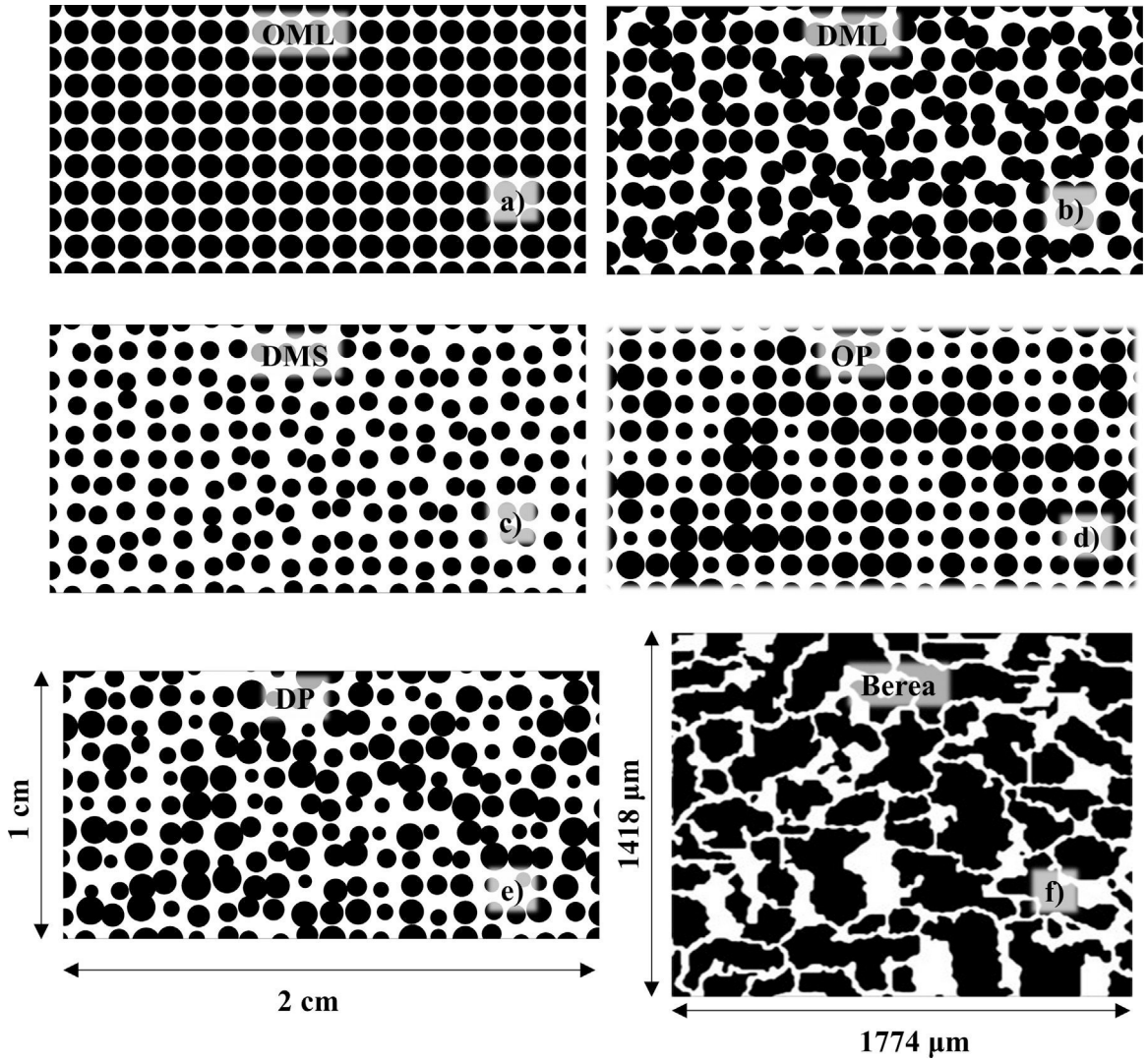


**Fig. 1.** 2D micromodels used in the present numerical simulations: (a) Ordered Monodisperse Large grains: OML, (b) Disordered Monodisperse Large grains: DML, (c) Disordered Monodisperse Small grains: DMS, (d) Ordered Polydisperse grains: OP, (e) Disordered Polydisperse grains: DP and (f) Berea sandstone micromodel. Black colour represents the solid grains and white colour represents the interstices. These geometries were obtained from [Mehmani and Tchelepi \(2017a\)](#) and are freely available ([Mehmani and Tchelepi, 2017b](#)).

**Table 1**

Main features of the investigated micromodels. The original names given by [Mehmani and Tchelepi \(2017a,b\)](#) to these micromodels are listed in the second column.

Medium	Original name	Level of disorder	Grain size	Grain shape	$\epsilon$ (%)	$K$ ( $m^2$ )	$T_N$
OML	GL - D1	Low	Monodisperse - Large	Circular	36.40	$5.51 \times 10^{-12}$	1.012
DML	GL - D4	High	Monodisperse - Large	Circular	38.97	$3.31 \times 10^{-10}$	1.456
DMS	GS - D4	High	Monodisperse - Small	Circular	61.97	$5.42 \times 10^{-9}$	1.160
OP	P - D1	Low	Polydisperse	Circular	47.78	$9.97 \times 10^{-10}$	1.309
DP	P - D4	High	Polydisperse	Circular	48.91	$1.60 \times 10^{-9}$	1.348
Berea	Berea	From rock sample	From rock sample	From rock sample	33.61	$3.87 \times 10^{-12}$	1.300

The original names given by [Mehmani and Tchelepi, \(2017a;b\)](#) to the investigated media have been modified in order to facilitate the current analysis. It is highlighted that the effect of grain size will be analysed by keeping the positions of the grains centers unchanged in both DML and DMS. Regarding the level of disorder, high disorder level was generated by randomly perturbing grain positions in both horizontal and vertical coordinates with respect to the low disorder level in which the grain centres are aligned.

In order to carry out further investigations on the microstructures, an equivalent pore network model representing each 2D porous medium was extracted. Pore network models are idealized

representations of the real porous geometry that reduce the complexity involved in solving transport problems at the pore scale. Moreover, essential features for permeability and pressure loss prediction, such as pore-body to pore-throat aspect ratio and pore connectivity, can be well characterized by the pore network models in typical cases ([Paul et al., 2019](#)). A review of the advances in pore network modelling of porous media was presented by [Xiong et al. \(2016\)](#), who described the different current applications ranging from dissolution phenomena to biomass growth. The pore network extraction operations carried out in the current work were performed using the subnetwork of the oversegmented wa-

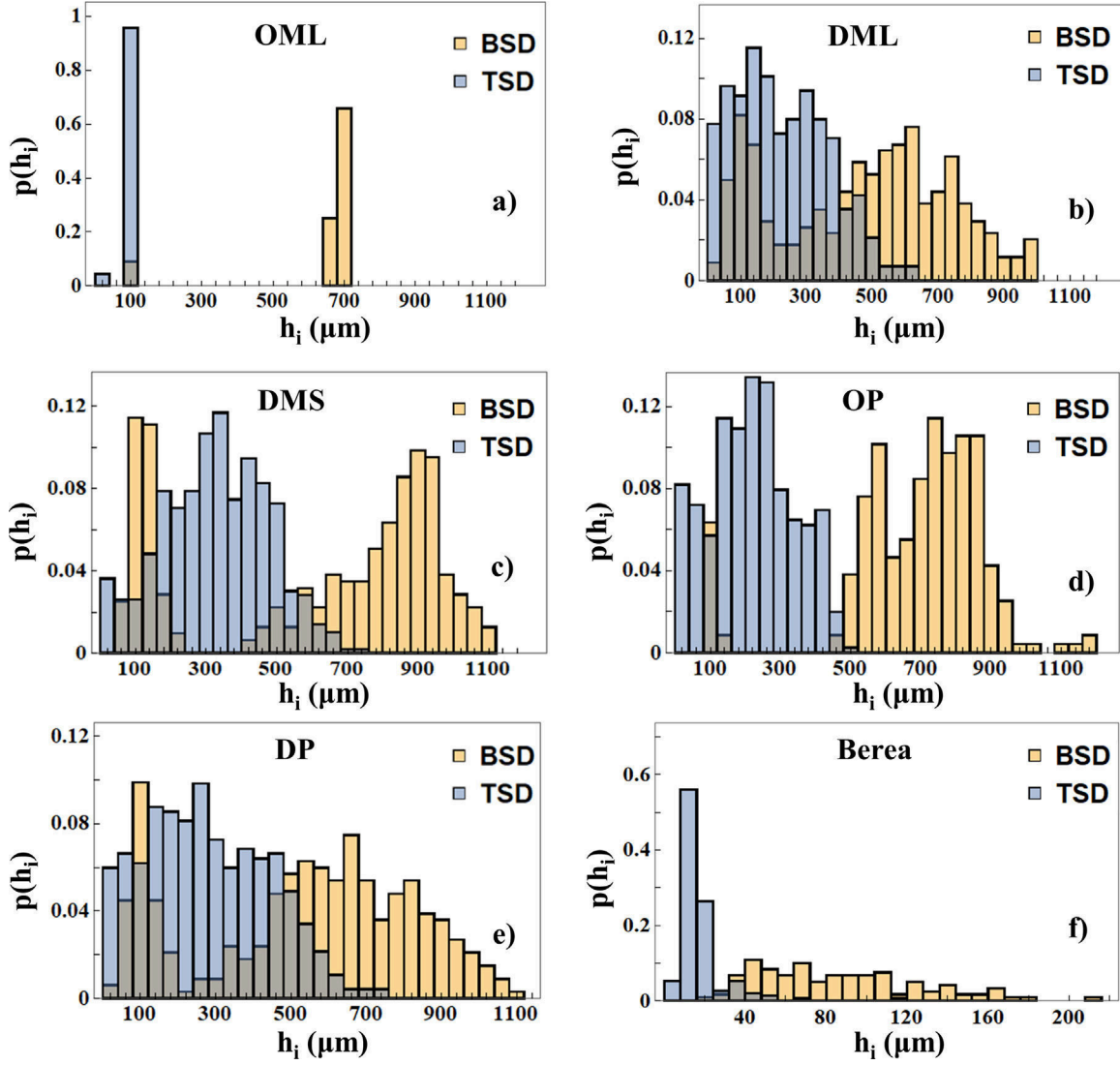


Fig. 2. Body Size Distributions and Throat Size Distributions of the six porous media investigated in the present work: (a) OML, (b) DML, (c) DMS, (d) OP, (e) DP and (f) Berea.

tershed (SNOW) algorithm (Gostick, 2017) implemented within the open-source toolkit for quantitative analysis of porous media images, PoreSpy (Gostick et al., 2019; Khan et al., 2019). The algorithm proceeds through different steps. It first extracts the distance map of the void spaces, filters it and eliminates peaks on saddles and plateaus and then merges peaks that are close to each other. Finally, it assigns void voxels (or pixels for a 2D medium) to pores. The SNOW algorithm was used for the extraction of the pore networks from the 2D media shown on Fig. 1. It is highlighted that the position of the centers of the grains remains unchanged for a given level of disorder in the investigated porous media. Therefore, the different combinations of grain size, grain shape, level of disorder and polydispersity produce changes in the compacity of the investigated media, and consequently in their porosity. The individual effects of such a porosity variation on yielding behavior and tortuosity are not specifically addressed in the current study. Also, it is noted that the average grain size of the polydisperse media is identical to the grain size of the monodisperse media with large grains.

The Body Size Distributions (BSD) and the Throat Size Distributions (TSD) of the pore-network models extracted from the six

porous media are represented in Fig. 2. Furthermore, in order to facilitate the analysis, the average throat size,  $m_{\text{throats}}$ , the standard deviation of the TSD,  $\sigma_{\text{throats}}$ , the average body size,  $m_{\text{bodies}}$ , and the standard deviation of the BSD,  $\sigma_{\text{bodies}}$ , were determined and are listed in Table 2. A noteworthy feature is the single probability peak obtained in both BSD and TSD of OML. Also, the pore dimensions of the Berea micromodel are significantly smaller than those of the other samples. It can be observed that the standard deviations of the BSDs and TSDs of the polydisperse media OP and DP are higher than those of the monodisperse media OML and DML, as expected from the diversity of grain sizes present in polydisperse media. Moreover, both  $m_{\text{bodies}}$  and  $m_{\text{throats}}$  are higher in the polydisperse media for a given level of disorder. The effect of grain size on pore characteristics can be evaluated by comparing the BSD and TSD obtained for DMS and DML. By doing so, it was observed that despite similar standard deviations, the values of  $m_{\text{throats}}$  and  $m_{\text{bodies}}$  were smaller for the porous medium with larger grain sizes. Another key aspect is the effect of disorder. Indeed, while partial overlap between TSD and BSD is obtained for the disordered media DML and DP, this effect is much less significant for the ordered ones.

**Table 2**

Average values and standard deviations of the BSDs and TSDs of the pore-networks extracted from the different porous media.

Medium	$m_{\text{throats}} (\mu\text{m})$	$\sigma_{\text{throats}} (\mu\text{m})$	$\sigma_{\text{throats}} (\%)$	$m_{\text{bodies}} (\mu\text{m})$	$\sigma_{\text{bodies}} (\mu\text{m})$	$\sigma_{\text{bodies}} (\%)$
OML	96	19	20	627	167	27
DML	222	141	64	474	258	54
DMS	322	149	46	618	342	55
OP	217	120	55	685	208	30
DP	274	164	60	540	282	52
Berea	17	13	76	86	40	47

## 2.2. Numerical experiments procedure

The procedure previously presented by [Rodríguez de Castro and Agnaou \(2019\)](#) was adopted in the present numerical simulations. In this procedure, the flow problems were numerically solved using the finite-element-method-based simulation package [Comsol Multiphysics version 5.3. \(2017\)](#). The porous media displayed in [Fig. 1](#) were discretized using unstructured triangle dominated meshes. The simulations were carried out using the *Creeping Flow* module, developed for solving Stokes flow problems. The boundary conditions associated with the flow problem consist of the Dirichlet uniform pressure at the left and right boundaries of the porous structures. In addition, a no-slip velocity condition was imposed at the grain-fluid interface as well as at the top and the bottom boundaries of the considered porous media. It was observed that, given the small ratio between the average grain size and the dimensions of the computational domain, the choice of boundary conditions at the top and bottom walls had not significant influence on the results. Also, it must be noted that since flow is induced thanks to the enforced pressure difference, backflow may appear at the inlet and result in numerical instabilities. For this reason, the backflow at the entrance (left boundary) was systematically eliminated. This constraint can be compared to the situation where one uses a pump to inject the fluid through the porous medium and where the pump does not allow the fluid to go back. The average skewness of the generated meshes ranged from 0.798 to 0.828. Regarding the resolution of the boundary layers along the walls of the pore channels, a minimum mesh element size of 20  $\mu\text{m}$  was used for all porous media apart from Berea sandstone, for which 3  $\mu\text{m}$  was imposed. This led to an average of 240 grid nodes per pore.

The fundamental character of yield stress fluids is that they flow only if they are submitted to a shear stress exceeding some critical value  $\tau_0$  ([Coussot, 2014](#)). Otherwise, they deform in a finite way like elastic solids. The rheological behavior under shear of such fluids is mostly described by the empirical Herschel-Bulkley law ([Herschel and Bulkley, 1926](#)). This law combines yield stress with a shear-dependent viscosity and, for simple shear, can be written as:

$$\begin{cases} \tau = \tau_0 + k\dot{\gamma}^n & \text{for } \tau \geq \tau_0 \\ \dot{\gamma} = 0 & \text{for } \tau \leq \tau_0 \end{cases} \quad (3)$$

where  $\tau_0$  is the yield stress,  $k$  is the consistency index and  $n$  is the fluidity index. To overcome the expected singularities when using such a relationship in numerical computations, the shear viscosity of the fluid was described as follows:

$$\mu = \begin{cases} \min\left[\mu_{\max}, \left(k\dot{\gamma}^{n-1} + \frac{\tau_0}{\dot{\gamma}}\right)\right] & \text{for } \dot{\gamma} > 0 \\ \mu_{\max} & \text{for } \dot{\gamma} = 0 \end{cases} \quad (4)$$

in which  $\mu_{\max}$  is a pre-defined maximum viscosity. A value  $\mu_{\max} = 10000 \text{ Pa s}$  was used in this study. It should be highlighted, however, that this maximum limit was adopted as a compromise between accuracy and numerical stability. On the one hand, using extremely high  $\mu_{\max}$  values yields important viscosity gradi-

ents within the computational domain and therefore numerical instabilities. On the other hand, low  $\mu_{\max}$  values fail to accurately reproduce the expected rheological behaviour. The resulting system of non-linear equations was solved using the *Comsol Stationary Solver* and the solution was sought using the Newton-Raphson algorithm, taking as initial guesses the initial conditions (fluid at rest, zero pressure and velocity fields). The system of linearized equations within each Newton-Raphson iteration, was solved using the direct solver PARDISO (Schenk, 2004). The numerical solution is then judged converged upon reaching a residual below a relative tolerance of  $10^{-3}$  both in terms of velocity and pressure. A computer equipped with an Intel(R) Core(TM) i7-4500U CPU node at 2.40GHz with 4 cores was used to perform the current numerical simulations. The simulation times were close to 20 min in all cases, with a memory usage of 4 GHz.

A first set of experiments was performed by using a yield stress fluid with shear-rheology parameters  $\tau_0 = 10 \text{ Pa}$ ,  $k = 1 \text{ Pa s}^n$  and  $n = 0.5$ . In these experiments, the yield index  $Y$  of the fluid was defined as the complement of the ratio between the computed surface-averaged shear viscosity  $\bar{\mu}$  and  $\mu_{\max}$  at each value of the imposed pressure gradient:

$$Y = 1 - \frac{\bar{\mu}}{\mu_{\max}} \quad (5)$$

$Y$  was used to quantify the size of the unyielded region. The value of  $Y$  is zero when the fluid is "stagnant" within the whole porous medium, and it approaches unity when the fluid flows with low viscosity in all pores. The numerical simulations were also used to obtain sets of average velocity vs. pressure gradient data points. For each imposed pressure gradient  $\nabla P_j$ , the resulting average velocity  $u_j$  was computed as the line integration over the inlet of the velocity component in the main flow direction divided by the width of the medium. Then, by using the computed  $(u_j, \nabla P_j)$  data, the apparent viscosity of the yield stress fluid in the porous medium  $\mu_{\text{app}}$  was calculated from Darcy's law ([Darcy, 1856](#)):

$$\mu_{\text{app}} = K \frac{\nabla P_j}{u_j} \quad (6)$$

The apparent shear rate  $\dot{\gamma}_{\text{app}}$  was subsequently calculated by using  $\mu_{\text{app}}$  as an input to Herschel-Bulkley's empirical law ([Herschel and Bulkley, 1926](#)), which can be rewritten as follows:

$$\mu_{\text{app}} = \frac{\tau_0}{\dot{\gamma}_{\text{app}}} + k\dot{\gamma}_{\text{app}}^{n-1} \quad (7)$$

In each experiment, the Herschel-Bulkley number  $H$ , also known as generalized Bingham number, was used to quantify the relative importance of yield stress  $\tau_0$  as compared to the excess shear stress  $k\dot{\gamma}_{\text{app}}^n$  produced in the power-law-viscosity regime ([Magnin and Piau, 2004](#); [Kandasamy and Nadiminti, 2015](#); [Moreno et al., 2016](#)):

$$H = \frac{\tau_0}{k\dot{\gamma}_{\text{app}}^n} \quad (8)$$

Furthermore, the hydraulic tortuosity values of the flow paths followed by Newtonian and yield stress fluids were also obtained

**Table 3**  
Herschel–Bulkley parameters of the fluids used in the present numerical simulations.

Fluid name	Standard	Low $\tau_0$	High $\tau_0$	Low k	High k	Low n	High n
$\tau_0$	10 Pa	1 Pa	100 Pa	10 Pa	10 Pa	10 Pa	10 Pa
k	1 Pa s <sup>n</sup>	1 Pa s <sup>n</sup>	1 Pa s <sup>n</sup>	0.1 Pa s <sup>n</sup>	10 Pa s <sup>n</sup>	1 Pa s <sup>n</sup>	1 Pa s <sup>n</sup>
n	0.5	0.5	0.5	0.5	0.5	0.33	1

from the post processing of the direct numerical simulation results. This was achieved by dividing the surface average of the velocity magnitude field  $|\bar{\mathbf{u}}|$  by the surface average of the horizontal component of velocity  $\bar{u}_x$  (since the imposed pressure gradient was oriented along the inverted x axis) over the pore space (Duda et al., 2011; Zhao et al., 2018; Zhang et al., 2019), with  $\mathbf{u}$  being the velocity vector:

$$T = \frac{|\bar{\mathbf{u}}|}{\bar{u}_x} \quad (9)$$

The same procedure was used in order to conduct a second set of *in silico* experiments, in which the injection of seven yield stress fluids with different Herschel–Bulkley parameters through the micromodel DP was simulated. Table 3 lists the Herschel–Bulkley parameters of the considered yield stress fluids. The results of this second set of experiments are presented in Section 3.1.4.

The definition of the tortuosity given by Eq. (9) is more rigorous and simpler than the more common definition  $T = L_e/L$ . In fact, this definition does not require the computation of the flow streamlines. It was shown (Duda et al., 2011) that T given by Eq. (9) is equivalent, for an incompressible flow without recirculation zones, to the surface (for a 3D configuration) average of  $L_e/L$  weighted by the local flux over a reference surface perpendicular to the main flow direction. This implies that if one uniformly discretizes the reference surface, the flux can be replaced by the velocity component normal to the reference surface. On the other hand, in the presence of recirculation zones, T given by Eq. (9) becomes an upper limit of the surface (over a reference surface) average of  $L_e/L$  weighted by the local flux.

### 3. Results

This section presents the results provided by the numerical simulations presented above. Sections 3.1.1, 3.1.2 and 3.1.3 deal with the injection of the investigated standard yield stress fluid through the different porous media, in order to assess the effects of microstructure on the hydraulic tortuosity and yielding behaviour. The second set of experiments in which a set of different yield stress fluids were injected in the same porous medium are presented in Section 3.1.4, aiming to evaluate the effects of varying Herschel–Bulkley parameters on Y and T.

#### 3.1. Computed $u$ ( $\nabla P$ ) data points and examples of the obtained shear viscosity and velocity maps

The computed  $u$  ( $\nabla P$ ) data obtained for the injection of the standard fluid ( $\tau_0 = 10$  Pa,  $k = 1$  Pa s<sup>n</sup> and  $n = 0.5$ ) through the set of porous media investigated in the current work are represented in Fig. 3(a). The unexpected trend observed at the lowest  $\nabla P$  values for OML and OP, where  $u$  is roughly proportional to  $\nabla P$ , is due to the existence of an important residual Newtonian flow produced below yielding in these ordered media, with viscosity  $\mu_{\max}$  (Eq. 2). Apart from this aspect, the  $u$  ( $\nabla P$ ) behaviour is the usual one for a yield stress fluid flowing through a porous medium (Rodríguez de Castro et al., 2016). Besides, it is reminded that, as mentioned in Section 2.2., Y can be used to quantify the size of the unyielded region. In order to facilitate the understanding of the relationship between the controllable macroscopic quan-

tity  $\nabla P$  and the measured dimensionless number Y, the Y vs.  $\nabla P$  results obtained for all numerical experiments are represented in Fig. 3(b). As expected, higher values of Y are obtained as  $\nabla P$  is increased, and once  $Y \sim 0.8$  is attained, a considerable increase in  $\nabla P$  is required to achieve the flow of the yield stress fluid within the whole porous medium ( $Y = 1$ ). In Fig. 4, examples of shear viscosity maps at intermediate values of Y are displayed over the three considered porous structures showing the existence of an important channelling effect through the largest pores. Furthermore, illustrative examples of the computed velocity maps are provided in Fig. 5 for different values of the Herschel–Bulkley number H, confirming that significant velocity magnitudes are obtained only in those pores in which the fluid has yielded. Also, as H decreases ( $\nabla P$  increases), the unswept area becomes smaller.

#### 3.2. Effects of the pore structure on the yielding behaviour of the fluid

The viscosity maps provided by the numerical simulations presented in subsection 3.1.1. for the flow of the standard Herschel–Bulkley fluid (Table 3) were used to calculate Y and H under different pressure gradients using Eqs. (5) and (8). From these results, the relationship between Y and H was determined and is represented in Fig. 6. It is noted that, in all cases, Y decreases when H is increased. This was expected due to the higher influence of yield stress at the high values of H (corresponding to small pressure gradients), leading to larger sizes of the unyielded regions (Prashant, 2011). More importantly, the main conclusion is that the relationship between Y and H depends on the type of structure. Moreover, in all cases, Y is lower than 0.2 when H is higher than 100, which means that a very small portion of the fluid is flowing at a significant velocity.

From Fig. 6(b), it can be deduced that the range of H over which progressive yielding is produced is shorter for the porous medium with small grains (and larger pores). This can be explained by the fact that, although the maximum throat sizes of DMS (small grains) and DML (large grains) are very close (Fig. 2), the TSD of DML presents higher probabilities for small pore sizes. Indeed, the fluid is mobilized in these small pores only at high pressure gradients, corresponding to lower values of H. Also, the considerably higher porosity of DMS is expected to facilitate yielding of the fluid at lower pressure gradients (higher values of H) as compared to DML. Moreover, it can be observed in Fig. 6(c) and 6(d) that the effect of polydispersity on the Y – H relationship is stronger for the ordered media, probably as a consequence of the marked differences in terms of TSD and BSD between the monodisperse and polydisperse ordered media. Fig. 6(f) shows that the influence of disorder on the Y – H relationship is negligible for the polydisperse media, while it is significant for the monodisperse media. This behaviour can be explained by the exceptional straightness of the flow paths obtained in OML, which results in a more abrupt yielding transition, as will be discussed in Section 4.

#### 3.3. Influence of the pore structure on the tortuosity of the streamlines

The hydraulic tortuosity of the streamlines was calculated for the flow of the considered standard Herschel–Bulkley fluid as well

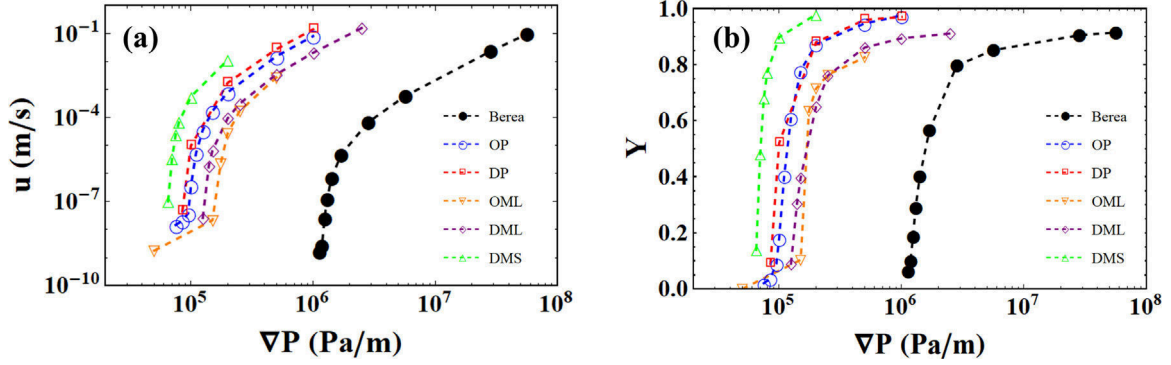


**Fig. 3.** (a) Simulated  $(u, \nabla P)$  data points and (b)  $Y$  vs.  $\nabla P$  relationship obtained for the injection of the standard fluid ( $\tau_0 = 10$  Pa,  $k = 1$  Pa  $s^n$  and  $n = 0.5$ ) through the different porous media investigated in the current work.

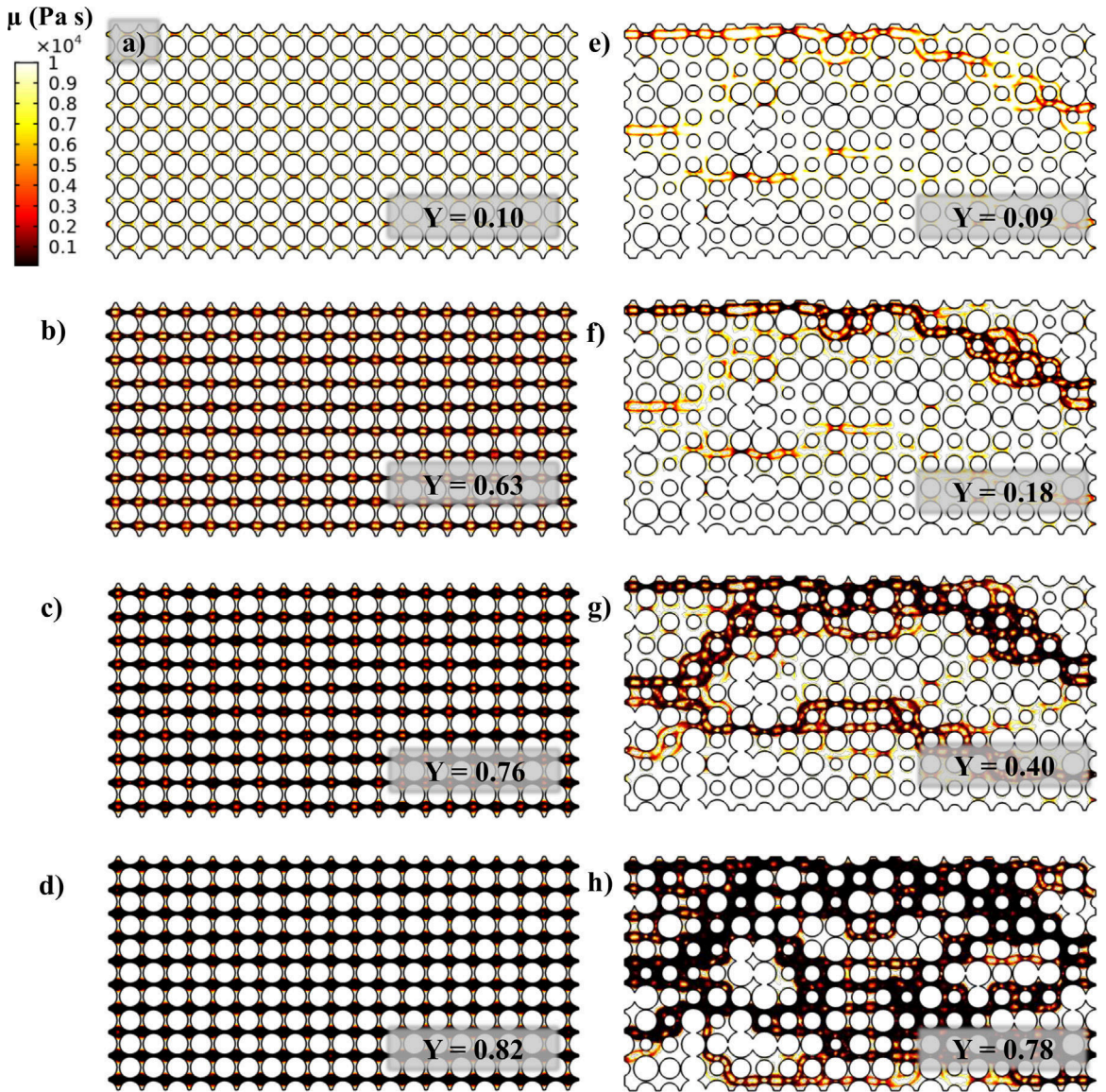


**Fig. 4.** Examples of shear viscosity maps as provided by the numerical simulations for different values of  $Y$  during the injection of the standard fluid ( $\tau_0 = 10$  Pa,  $k = 1$  Pa  $s^n$  and  $n = 0.5$ ): (a - d) correspond to the porous medium OML and (e - h) to the porous medium OP.



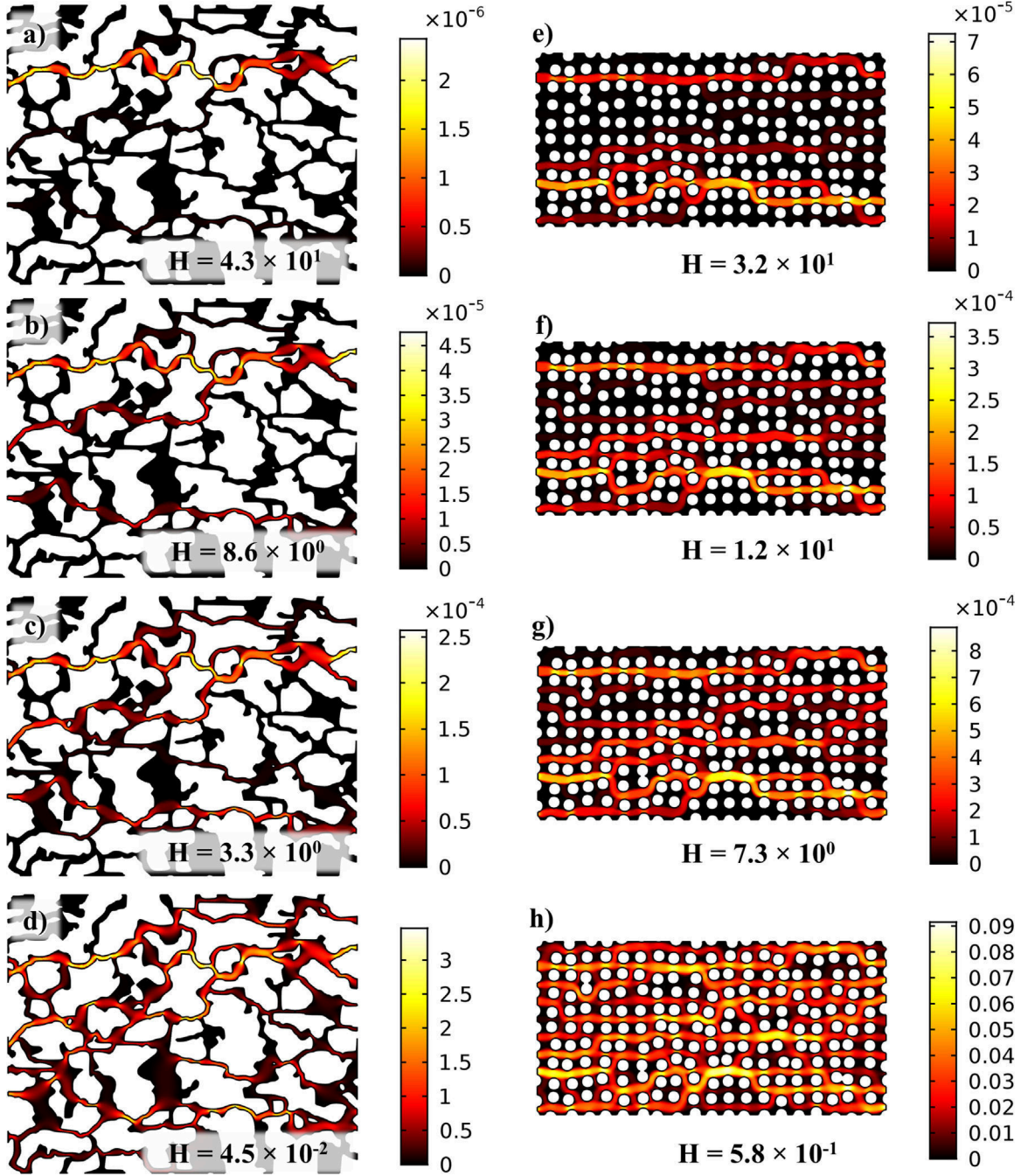


**Fig. 5.** Examples of simulated velocity maps obtained for different values of  $H$  during the injection of the standard fluid ( $\tau_0 = 10$  Pa,  $k = 1$  Pa sn and  $n = 0.5$ ). (a – d) correspond to Berea sandstone and (e – h) to the porous medium DMS. The colour scale represents the magnitude of velocity at each position. The values in the colorbars are expressed in  $m\ s^{-1}$ .

as for a Newtonian fluid by using Eq. (9), and its dependence on  $Y$  was investigated. Fig. 7 shows that the hydraulic tortuosity of the flow of the Herschel–Bulkley fluid is lower than that of a Newtonian fluid for all the tested porous media, except for the ordered monodisperse medium OML for which they coincide (Fig. 7c and 7e). This is true even when  $Y$  approaches unity, i.e., when  $H$  becomes very low and the effect of yield stress is well mitigated. Such low tortuosity stems from the directional nature of shear-thinning behaviour and yielding. Indeed, the shear viscosity decreases as the applied pressure gradient increases. Consequently, low viscosity regions are oriented along the main direction of the flow, where the pressure gradients are higher than in transverse directions, as clearly illustrated in Fig. 4. In the particular case

of OML, in which all grains are perfectly aligned, the flow paths offering the lowest resistance to flow correspond to the shortest ones, i.e., straight lines going from the inlet to the outlet of the medium traveling over the identical pore constrictions with a hydraulic tortuosity approaching unity both for the Newtonian and the yield stress fluid flows. For the other considered porous media, including the Berea sandstone micromodel, hydraulic tortuosity is observed to increase with decreasing  $Y$  within the low  $Y$ -regime. This is expected to be related to the Newtonian viscosity limit  $\mu_{max}$  imposed during the flow simulations. Indeed, the residual Newtonian flow with viscosity  $\mu_{max}$  becomes more significant as  $Y$  approaches zero, and therefore the higher tortuosity of the residual Newtonian flow ( $T_N$ ) in some regions of the mi-

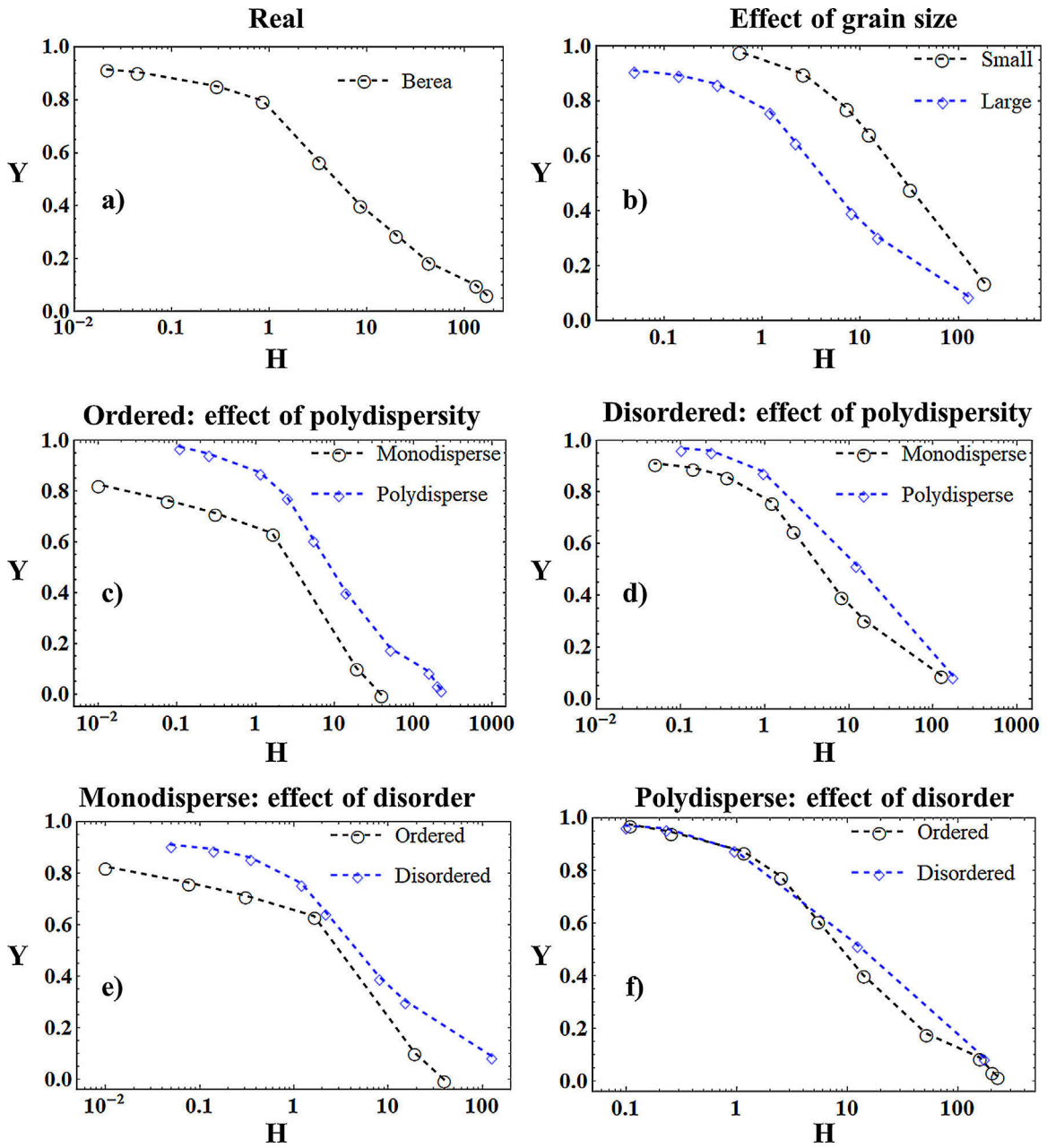


**Fig. 6.** Relationships between yield index,  $Y$ , and Herschel–Bulkley number,  $H$ , for the different porous media during the injection of the standard fluid ( $\tau_0 = 10$  Pa,  $\mathbf{k} = 1$  Pa s  $n$  and  $n = 0.5$ ). (a) Berea sandstone. (b) Effect of grain size by comparing DMS (small grain size) and DML (large grain size). (c) Effect of polydispersity in ordered porous media by comparing OML (monodisperse) and OP (polydisperse). (d) Effect of polydispersity in disordered porous media by comparing DML (monodisperse) and DP (polydisperse). (e) Effects of disorder in monodisperse porous media by comparing OML (ordered) and DML (disordered). (f) Effects of disorder in polydisperse porous media by comparing OP (ordered) and DP (disordered).

chromodel contribute to increase the average value of  $T$  throughout the medium. The preceding finding is in good agreement with the results of Zhang et al. (2019) for Cross fluids. It should be emphasized that, although ideal Herschel–Bulkley fluids do not exhibit any viscosity plateau at very low shear rates, the use of  $\mu_{\max}$  is quite realistic in the case of most commonly encountered pseudo-yield stress fluids, as previously shown and discussed by several researchers (Spelt et al., 2005; Lavrov, 2013; Rodríguez de Castro et al., 2018). Besides this, the main flow features are as follows:

- The hydraulic tortuosity dependence on  $Y$  is weaker for the porous media with the narrowest TSDs (Table 2), i.e., OML and DMS. This is because of the number of preferential flow paths is smaller and the increase of  $Y$  (at higher  $\nabla P$ ) occurs under

the same flow configuration, leading to an almost constant  $T$ .

- The polydispersity of the grain size distribution leads to an overall increase in hydraulic tortuosity in the ordered media (Fig. 7c). As described by Kostenko and Talon (2019), this is due to the diversion of the flow produced by the considerable increase in the magnitude of the permeability of local highly permeable zones.
- The tortuosity of the disordered polydisperse medium DP is lower than the one of the disordered monodisperse medium DML (Fig. 7d). This is possibly due to the similar range of sizes covered by the TSDs and the BDSs of both disordered media and the significant overlap between their TSD and BDS (Fig. 2). As a result, the maximum local permeability is not necessarily higher for the polydisperse medium.

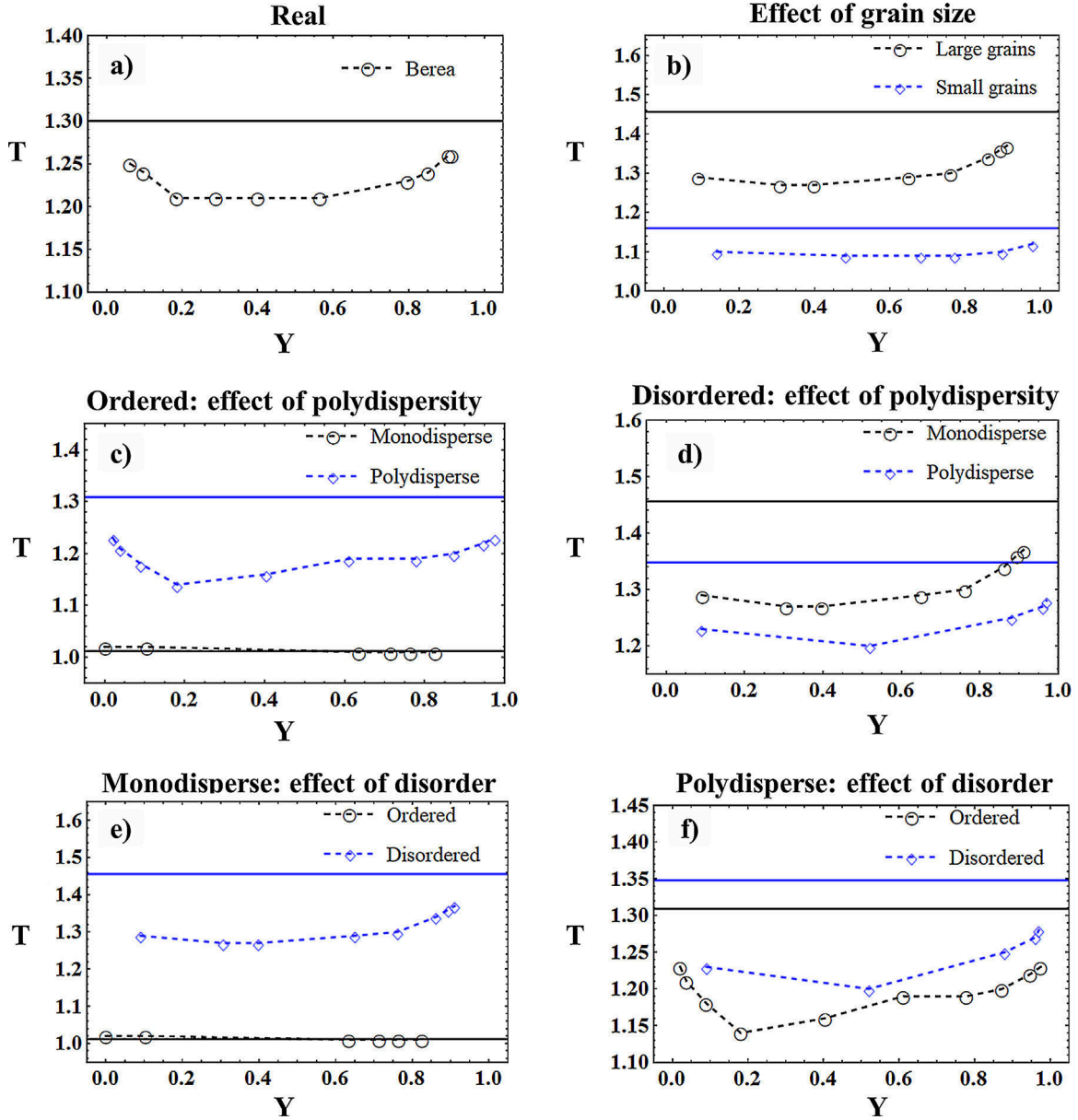


**Fig. 7.** Relationships between Hydraulic tortuosity and yield index for the different porous media during the injection of the standard fluid ( $\tau_0 = 10$  Pa,  $k = 1$  Pa s<sup>n</sup> and  $n = 0.5$ ). The continuous lines represent the constant hydraulic tortuosity  $T_N$  for Newtonian flow in each case, while dashed lines correspond to the flow of the yield stress fluids. (a) Berea sandstone. (b) Effects of grain size by comparing DMS (small) and DML (large). (c) Effects of polydispersity in ordered porous media by comparing OML (monodisperse) and OP (polydisperse). (d) Effects of polydispersity in disordered porous media by comparing DML (monodisperse) and DP (polydisperse). (e) Effects of disorder in monodisperse porous media by comparing OML (ordered) and DML (disordered). (f) Effects of disorder in polydisperse porous media by comparing OP (ordered) and DP (disordered).

-  $T$  increases with  $Y$  at moderate and high values of  $Y$ , which is explained by the decreasing intensity of channelling displayed in Figs. 4 and 5, and the greater number of paths opening to the flow as the pressure gradient is increased. It is noted that no significant differences in such a behaviour were observed between media with different grain sizes.

It should be kept in mind that, while the present conclusions are valid for the considered configurations, further works are required in order to generalize these findings.

### 3.4. Effect of Herschel–Bulkley parameters on the yielding behaviour and the tortuosity of the streamlines

In an effort to elucidate the individual effects of  $\tau_0$ ,  $k$  and  $n$  on the investigated relationships, the results of the set of flow simula-

tions using different fluids (Table 3) are represented in Figs 8 and 9. All fluids were injected through the same porous medium, DP. As reported in Fig. 8,  $H$  monotonically decreases with  $\nabla P$  in all cases, as expected from Eqs. (6)–(8). More precisely, one can note that higher values of  $\tau_0$  consistently lead to higher values of  $H$  for a given pressure gradient. On the contrary, the effect of  $k$  is significant only for the lowest pressure gradients. This is because higher values of  $k$  lead to higher values of  $\mu_{app}$  under a given pressure gradient, leading, in turn, to smaller values of  $\dot{\gamma}_{app}$ . Consequently, the denominator of Eq.(8) remains roughly constant and the value of  $H$  is almost unaffected. Analogously, the fluidity index  $n$  has a growing influence on  $H$  as the pressure gradient decreases, which can be explained by employing a similar reasoning.

It is observed in Fig. 9a that the effect of the value of  $\tau_0$  on the dependence of  $Y$  on  $H$  is only significant for  $H > 1$ , e.g., at the

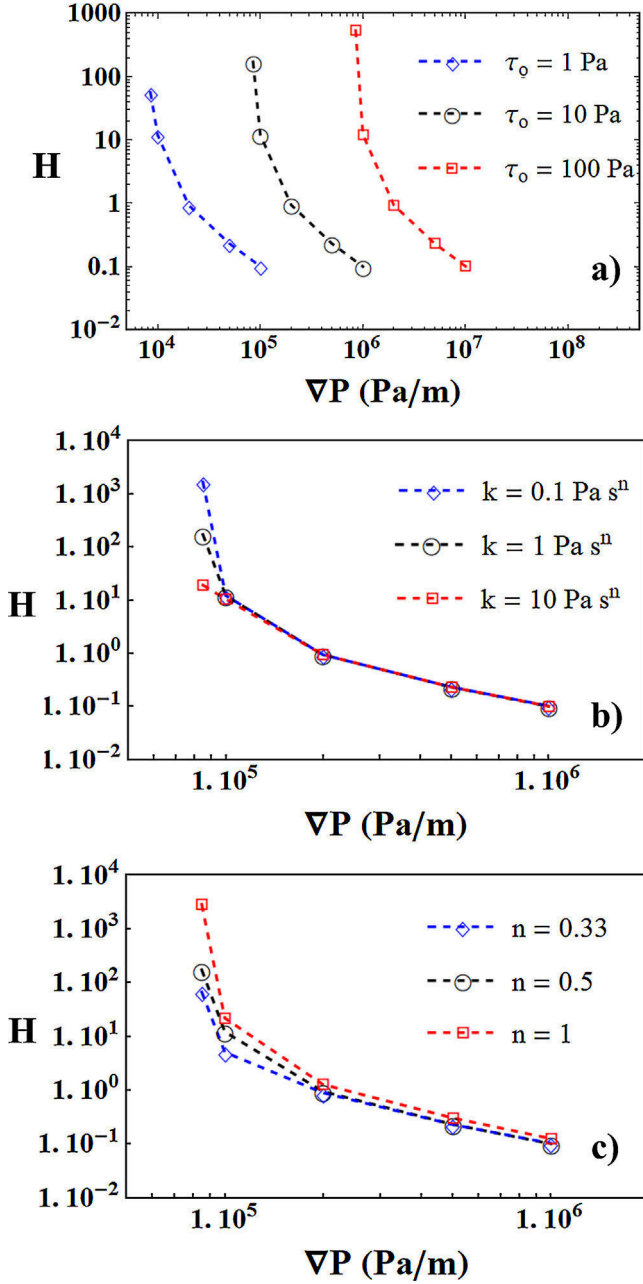


**Fig. 8.** Relationships between  $H$  and  $\nabla P$  for the different Herschel-Bulkley fluids (Table 3) injected through DP. (a) represents the dependence on  $\tau_0$ , (b) the dependence on  $k$  and (c) dependence on  $n$ .

lowest pressure gradients for which the fluid has still not yielded in many pores. Moreover, the onset of yielding (taken as  $Y = 0.2$ ) occurs at higher values of  $H$  when  $\tau_0$  is increased, and the intermediate values of  $Y$  span over a wider range of  $H$ . Indeed, in the presence of a yield stress, progressive yielding occurs between a minimum pressure gradient  $\nabla P_{\min} = 2\tau_0/h_{\max}$  and a maximum pressure gradient  $\nabla P_{\max} = 2\tau_0/h_{\min}$ , with  $h_{\max}$  and  $h_{\min}$  being characteristic sizes of the largest and the smallest constrictions in the medium. Therefore, the range between  $\nabla P_{\min}$  and  $\nabla P_{\max}$  is proportional to the value of  $\tau_0$ . This results in wider ranges of  $H$  as the value of  $\tau_0$  increases, in qualitative agreement with the results displayed in Fig. 9a. Also, it can be deduced from Fig. 9b that the value of  $H$  corresponding to a given value of  $Y$  becomes lower as  $k$  increases, with the intermediate stages of yielding spanning over

a narrower range of  $H$ . In this regard, it can be noted that despite  $\nabla P_{\min}$  and  $\nabla P_{\max}$  being unaffected by  $k$ , the value of the average shear viscosity  $\bar{\mu}$  (Eq. 3) under a given pressure gradient is higher as  $k$  increases, resulting in lower values of  $Y$ . In contrast, lower values of  $n$  increase the shear-thinning behaviour of the fluid, leading to lower values of  $\bar{\mu}$  and higher values of  $Y$  for a given  $H$ , as depicted in Fig. 9c.

The relationships between  $T$  and  $Y$  for the different combinations of Herschel-Bulkley parameters are also displayed in Fig. 9. A remarkable feature that can be deduced from these results is the lower hydraulic tortuosity of Herschel-Bulkley flow as compared to Newtonian flows, whatever the values of  $\tau_0$ ,  $k$  and  $n$ . Moreover,  $n$  is shown to be the only Herschel-Bulkley parameter that significantly affects the  $T$  vs.  $Y$  relationship, which stems from the stronger channelling effect exhibited by shear-thinning fluids of low fluidity index. Also, the increase in hydraulic tortuosity at the lowest values of  $Y$  is very similar for all the considered fluids.

#### 4. Discussion

In their investigation using non-yielding shear-thinning fluids, Zhang et al. (2019) reported an increase in  $T$  with increasing  $\nabla P$  at the highest values of the pressure gradient. This effect was attributed to the value of the high shear plateau viscosity  $\mu_\infty$  exhibited by the fluids investigated in that work (Cross power-law fluids) and also to the important inertial pressure drops. Based on this work, and since neither  $\mu_\infty$  nor the inertial pressure drops are considered in the present numerical experiments, one may expect no increase in  $T$  at the highest values of  $\nabla P$  (associated to the highest values of  $Y$ ). However, the opposite effect was proven in the present study, showing that  $T$  does increase at the highest values of  $Y$  (as shown in Figs. 7 and 9). As mentioned above, this is a direct implication of the decreasing intensity of channelling effect as a greater number of paths open to the flow of the yield stress fluid when the pressure gradient is increased.

It must be mentioned that, in the case of Direct Numerical Simulations (DNS), the governing equations are solved on the actual pore space geometry obtained through an imaging technique, such as X-ray microtomography. In contrast, only a simplified representation of the complex geometry of the pore space is used in Pore Network Modeling (PNM), usually consisting of a network of spherical pore bodies connected by cylindrical pore throats in which most pressure loss is generated. This important simplification makes PNM highly efficient from a computational point of view, especially when compared to more fundamental DNS, which are computationally expensive. Nevertheless, this geometric simplification also leads to secondary simplifications in the flow and transport physics, which result in a loss of predictive accuracy (Mehmani and Tchelepi, 2016; Xiong et al., 2016). Several authors studied the flow of shear-thinning fluid with and without yield stress in the past using mechanistic PNM (Sahimi, 1993; Tsakiroglou, 2002; Perrin et al., 2006; Sochi and Blunt, 2008; Balhoff et al., 2012), achieving a significant reduction in the computation times as compared to DNS. However, experimental validation of PNM results is still a challenge, particularly in the case of yield stress fluids (Sochi and Blunt, 2008). The discrepancies existing between PNM predictions and experimental datasets may be explained by the physical effects that have still not been modelled, such as precipitation and adsorption.

The Representative Elementary Volume (REV) of the analyzed porous media for the macroscopic quantities  $Y$  and  $T$  investigated in the present work was assumed to be smaller than the size of the computational domains used in the numerical simulations. In order to assess the validity of this assumption, the values of  $T$  and  $Y$  were computed for the same pressure gradient in 4 subregions of the DML and DP media having, respectively, 50%, 66%, 75% and 85%

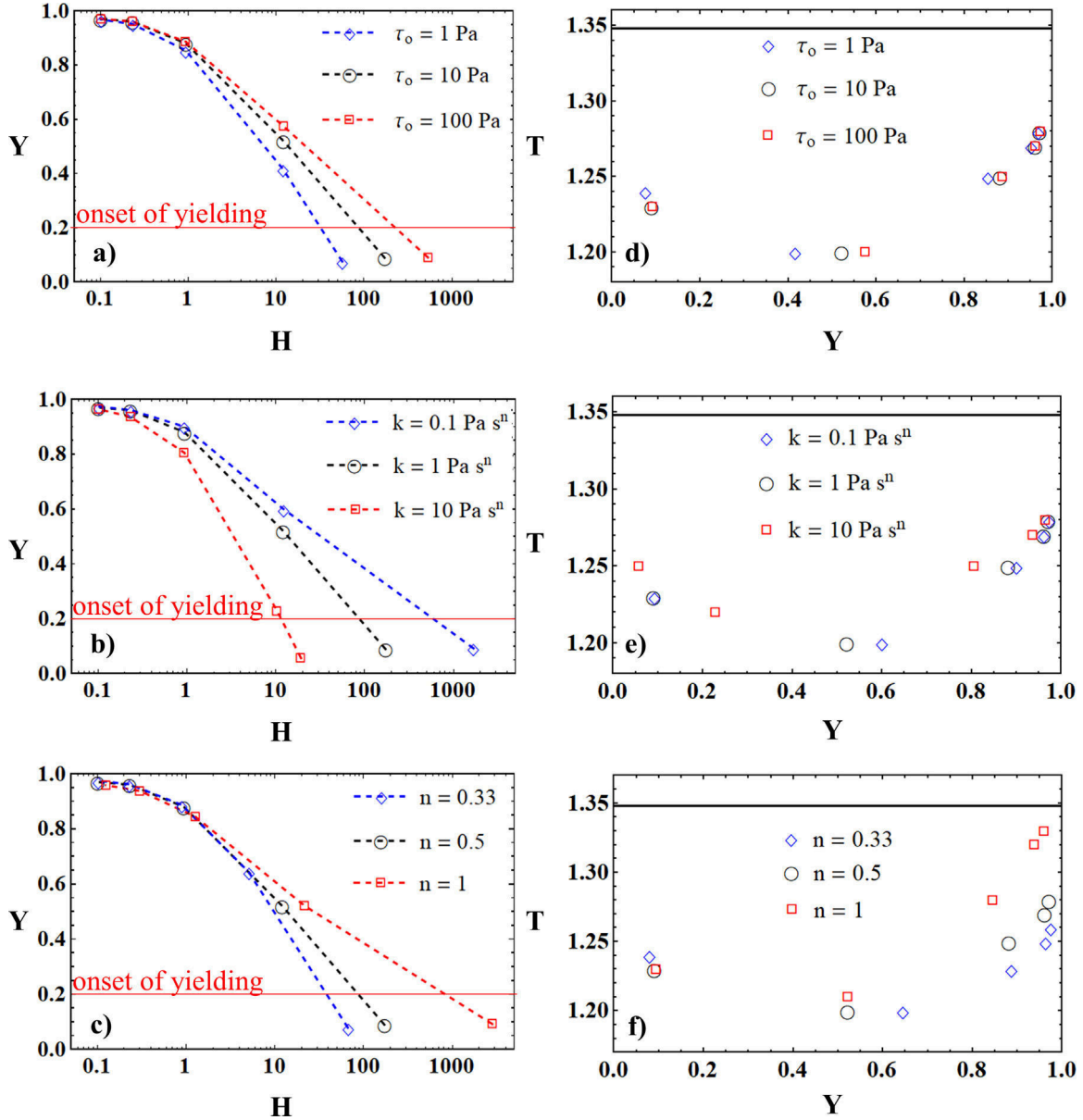


**Fig. 9.** Relationships between  $Y$  and  $H$  (a, b,c) and between  $T$  and  $Y$  (d, e, f) for the different Herschel-Bulkley fluids (Table 3) injected through DP. (a,d) represent the dependence on  $\tau_o$ , (b,e) the dependence on  $k$  and (c,f) dependence on  $n$ . The continuous black lines in figures (d), (e) and (f) represent the constant hydraulic tortuosity  $T_N$  for Newtonian flow. The onset of yielding according to the criterium  $Y = 0.2$  is represented by a continuous red line in figures (a), (b) and (c).

of the original size, and situated in the central part of the micro-models. From this analysis, it was concluded that only slight variation in the values of  $T$  and  $Y$  ( $\sim 10\%$  for  $Y$  and  $\sim 1\%$  for  $T$ ) occurred above 75% of the original size. Moreover, it should be noted that other authors (Lasseux et al., 2011) performed numerical simulations using 2D porous media of similar characteristics, reporting that a matrix of more than  $10 \times 10$  solid elements was representative for the calculation the macroscopic quantities ( $20 \times 10$  solid elements were used here). Also, the concept of REV and its determination from X-ray microtomography images were analyzed by Al-Raoush and Papadopoulos (2010).

Proper characterization of the Pore Size Distribution (PSD) of porous media is crucial in many industrial applications, e.g. separation processes, food industry, in situ remediation of contaminated soils, transport of landfill leachates, oil and gas industry,  $\text{CO}_2$  sequestration, transport of seawater through underground aquifers or

geothermal energy generation. Nowadays, the “gold standard” technique to characterize the PSD of porous materials is Mercury Intrusion Porosimetry (MIP), which presents well-known shortcomings, especially the environmental problems and health concerns arising from the use of toxic mercury as well as the severe restrictions on its use. As a safe alternative, the Yield Stress fluids Method (YSM) consists in computing the PSD of a given material from the pressure drop vs. flow rate measurements during injection of a given yield stress fluid. When defining the pore size class  $h_0$  that opens to the flow of the yield stress fluid under a pressure drop  $\Delta P_0$ , the algorithm of YSM technique (Rodríguez de Castro et al., 2014; 2016; 2018) assumes that the pores are straight and horizontal, with a length  $L$  equal to the length of the bundle. In contrast, the length of a real streamline with hydraulic tortuosity  $T$  is  $L_e = T \times L$ , and the depth of the tortuous channel opening to the flow under the same pressure drop  $\Delta P_0$  is  $h_0^* = h_0 T$ . Therefore,

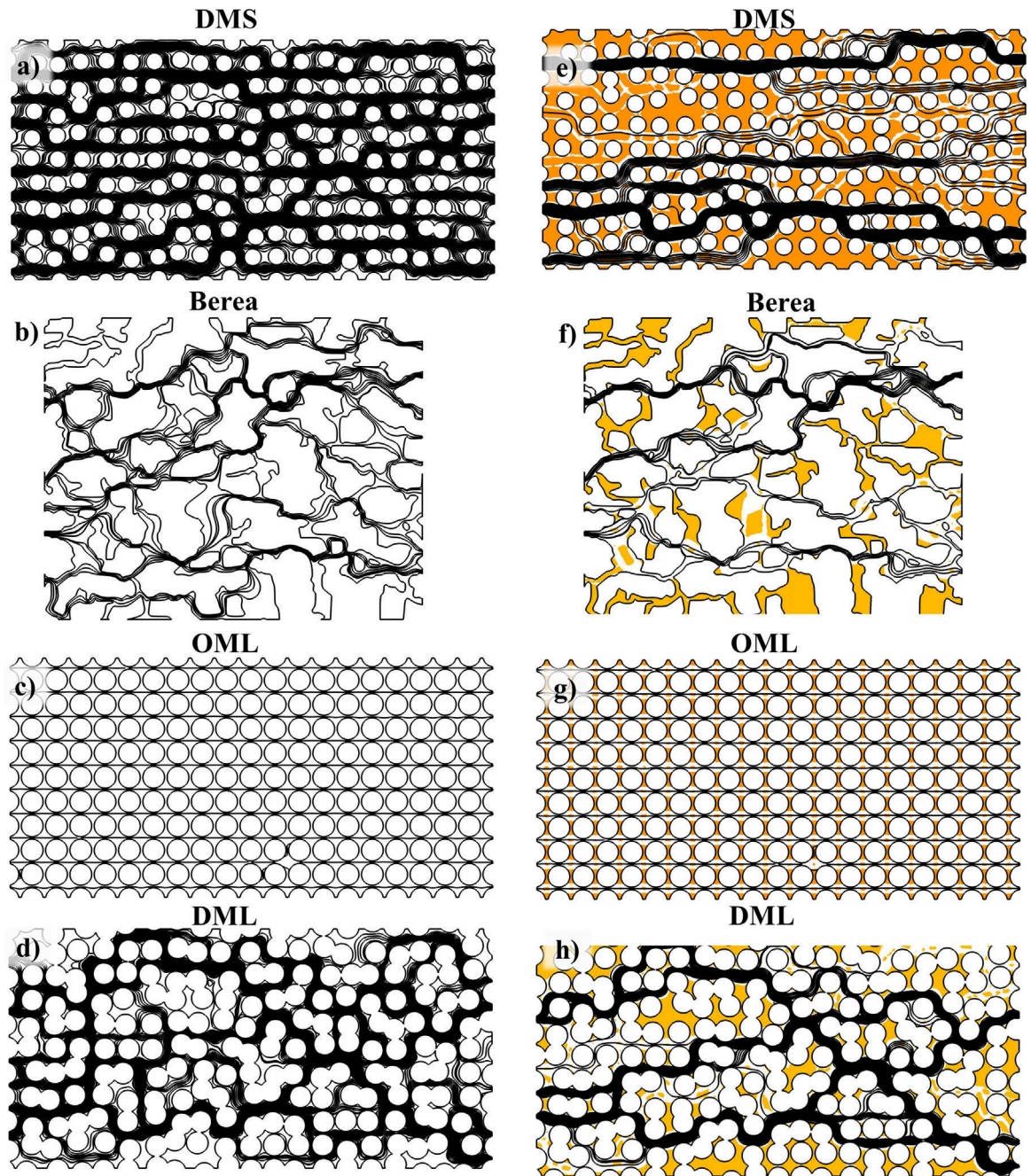


**Fig. 10.** Examples of streamlines for the flow a Newtonian fluid (a–d) and the yield stress fluid (e – h) through different porous media. The corresponding values of  $Y$  are: (e)  $Y = 0.48$ , (f)  $Y = 0.57$ , (g)  $Y = 0.63$ , (h)  $Y = 0.65$ .

including the dependence of  $T$  on flow rate is expected to improve the accuracy of the PSDs provided by Yield Stress fluids porosimetry Method (YSM). In order to illustrate the preceding aspect, the intricateness of the streamlines obtained in the case of the present simulations is shown in Fig. 10, confirming the existence of stagnant zones and questioning the assumption of straight streamlines used in YSM for all tested media apart from OML.

Given that the investigated media were 2D sections of 3D structures, comparison against experiments was not possible. However, microfluidic experiments in which a transparent yield stress fluid is displaced by a dyed one, similar to those performed by Auradou et al. (2008) in a rough fracture, may be an appropriate means to obtain experimental measurements of  $T$  which can be compared to the present numerical results

## 5. Conclusions and prospects

A key finding of the current work is the lower hydraulic tortuosity of yield stress fluid flow as compared to Newtonian fluid flow in porous media, due to the directional nature of yielding. Only the ordered porous medium is an exception to such a conclusion, which is explained by the straightness of the streamlines for all the tested fluids. Moreover, tortuosity has been shown to increase with increasing  $Y$  once the size of the stagnant region is reduced ( $Y > 0.4$  in the present experiments) and the impact of channelling is mitigated. Also, an increase in tortuosity is observed at the lowest pressure gradients in the presence of the viscosity limit  $\mu_{\max}$  imposed during the numerical simulations. Attention must be drawn to the strong effect of the size distribution of pore throats on the

variation of tortuosity at different yielding stages, which is a consequence of the influence of this microscopic characteristic on the diversity of preferential flow paths. Among the Herschel–Bulkley parameters, only the fluidity index has been observed to affect the tortuosity of the flow for a given level of yielding.

The dependence of the level of yielding has also been assessed as a function of the value of Herschel–Bulkley number  $H$  for the different micromodel–fluid combinations, and the following conclusions have been drawn:

- The level of yielding achieved at a given value of  $H$  depends on the structure of the porous medium.
- Yielding occurs over a wider range of  $H$  in the micromodel with smaller pores.
- Disorder plays a significant role in the relationship between yielding level and  $H$  only in the cases in which the size distribution of the solid grains is monodisperse.
- The influence of polydispersity on yielding behaviour is stronger in ordered media.
- The value of the yield stress strongly affects the range and values of  $H$  over which yielding occurs. Besides, high consistency and low fluidity indexes result in a decrease in the values of  $H$  covering such transition.

The conclusions of the present work can be used to significantly improve the accuracy of the models used for predicting pressure drops, local pore velocities and stagnant region size in yield stress fluid flows through porous media, by considering hydraulic tortuosity dependence on injection flow rate. Such detailed modelling is most valuable in a great number of industrial applications, e.g., in situ remediation of contaminated groundwater, filtration of polymeric liquids or liquid food engineering. The present study was carried out considering two-dimensional (2D) ordered and disordered model porous structures (Fig. 1), with different grain sizes and shapes. Since the objective was to examine the relationships between  $H$ ,  $T$  and the rheological parameters, 2D configurations extracted from a 3D structure were used. This was further motivated by the fact that accurate numerical simulations are more tractable, and their results can be more easily and more clearly interpreted in the 2D case. Moreover, a thorough analysis of 2D and three-dimensional (3D) flows of yield stress fluids in porous media (Talon and Bauer, 2013; Bauer et al., 2019) showed that the same flow regimes are observed in both cases.

Nevertheless, additional research and experiments are required in order to extend these results to the flow of yield stress fluids through 3D porous media. The main stumbling block to achieve this goal is the considerable computational power required to compute the pressure and velocity maps in the 3D case. In this regard, recent developments in pore–network modelling are expected to provide an effective alternative to direct numerical simulations in future studies. Also, given that the investigated media were 2D sections of 3D structures, comparison against experiments was not possible. However, microfluidic experiments in which a transparent yield stress fluid is displaced by a dyed one, similar to those performed by Auradou et al. (2008) in a rough fracture, may be an appropriate means to obtain experimental measurements of  $T$  which can be compared to the present numerical results

#### Declaration of Competing Interest

None.

#### CRediT authorship contribution statement

**Antonio Rodríguez de Castro:** Conceptualization, Methodology, Software, Formal analysis, Investigation, Writing - original draft, Visualization. **Mehrez Agnaou:** Software, Resources, Writing - review

& editing. **Azita Ahmadi-Sénichault:** Writing - review & editing. **Abdelaziz Omari:** Writing - review & editing.

#### References

- Agnaou, M., Lasseux, D., Ahmadi, A., 2017. Origin of the inertial deviation from Darcy's law: an investigation from a microscopic flow analysis on two-dimensional model structures. *Phys. Rev. E* 96, 043105.
- Al-Raoush, R., Papadopoulos, A., 2010. Representative elementary volume analysis of porous media using X-ray computed tomography. *Powder Technol.* 200, 69–77.
- Auradou, H., Boschan, A., Chertcoff, R., Gabbaneli, S., Hulín, J.P., Ippolito, I., 2008. Enhancement of velocity contrasts by shear-thinning solutions flowing in a rough fracture. *J. Non-Newtonian Fluid Mech.* 153, 53–61.
- Balhoff, M., Sánchez-Rivera, D., Kwok, A., Mehmani, Y., Prodanovic, M., 2012. Numerical algorithms for network modeling of yield stress and other non-Newtonian fluids in porous media. *Transp. Porous Media* 93, 363–379.
- Bao, K., Lavrov, A., Nilsen, H.M., 2017. Numerical modeling of non-Newtonian fluid flow in fractures and porous media. *Comput. Geosci.* 21, 1313–1324.
- Bauer, D., Talon, L., Peysson, Y., Ly, H. B., Bâton, G., Chevalier, T., Fleury, M., 2019. Experimental and numerical determination of Darcy's law for yield stress fluids in porous media. *Phys. Rev. Fluids* 4, 063301.
- Boek, E.S., Venturoli, M., 2010. Lattice-Boltzmann studies of fluid flow in porous media with realistic rock geometries. *Comput. Math. Appl.* 59, 2305–2314.
- Carman, P., 1937. Fluid flow through granular beds. *Chem. Eng. Res. Des.* 75 (December), S32–S48.
- Chevalier, T., Talon, L., 2015. Generalization of Darcy's law for Bingham fluids in porous media: from flow-field statistics to the flow-rate regimes. *Phys. Rev. E* 91, 023011.
- Chhabra, R.P., Richardson, J.F., 2008. *Non-Newtonian Flow and Applied Rheology: Engineering Applications*. Amsterdam; Boston: Butterworth-Heinemann/Elsevier.
- Clenell, M.B., 1997. *Tortuosity: A Guide Through the Maze (Special Publication)* 122, 299–344.
- COMSOL Multiphysics version 5.3. [www.comsol.com](http://www.comsol.com), COMSOL AB, Stockholm, Sweden (2017).
- Coussot, P., 2014. Yield stress fluid flows: a review of experimental data. *J. Non-Newtonian Fluid Mech.* 211, 31–49.
- Darcy, H.P.G., 1856. *Les fontaines publiques de la ville de Dijon*. Librairie des Corps Impériaux des Ponts et Chaussées et des Mines, Paris, pp. 590–594.
- Duda, A., Koza, Z., Matyka, M., 2011. Hydraulic tortuosity in arbitrary porous media flow. *Phys. Rev. E* 84 (3), 036–319.
- Dullien, F., 1992. *Porous Media Fluid Transport and Pore Structure*, 2nd ed Academic Press, New York.
- Ghanbarian, B., Hunt, A.G., Ewing, R.P., Sahimi, M., 2013. Tortuosity in porous media: a critical review. *Soil Sci. Soc. Am. J.* 77, 1461–1477.
- Gostick, J.T., 2017. Versatile and efficient pore network extraction method using marker-based watershed segmentation. *Phys. Rev. E* 96, 023307.
- Gostick, J.T., Khan, Z.A., Tranter, T.G., Kok, M.D., Agnaou, M., Sadeghi, M., Jervis, R., 2019. PoreSpy: a Python toolkit for quantitative analysis of porous media images. *J. Open Source Softw.* 4, 1296.
- Habisreuther, P., Djordjevic, N., Zarzalis, N., 2009. Statistical distribution of residence time and tortuosity of flow through open-cell foams. *Chem. Eng. Sci.* 64 (23), 4943–4954.
- Herschel, W.H., Bulkley, R., 1926. Konsistenzmessungen von Gummi-Benzollösungen. *Kolloid-Zeitschrift* 39, 291–300.
- Kandasamy, A., Nadiminti, S.R., 2015. *Int. J. Appl. Comput. Math.* 1, 235–249.
- Khan, Z.A., Tranter, T., Agnaou, M., Elkamel, A., Gostick, J., 2019. Dual network extraction algorithm to investigate multiple transport processes in porous materials: image-based modeling of pore and grain scale processes. *Comput. Chem. Eng.* 123, 64–77.
- Kostenko, R., Talon, L., 2019. Numerical study of Bingham flow in macroscopic two dimensional heterogeneous porous media. *Physica A* 528, 121501.
- Kozeny, J., 1927. *Über kapillare Leitung des Wassers im Bodeu*. Sitzungsberichte der Akadmie der Wissenschaftung in Wein Abteilung IIa 136, 271–301.
- Laudone, G.M., Gribble, C.M., Jones, K.L., Collier, H.J., Matthews, G.P., 2015. Validated a priori calculation of tortuosity in porous materials including sandstone and limestone. *Chem. Eng. Sci.* 131, 109–117.
- Lavrov, A., 2013. Non-Newtonian fluid flow in rough-walled fractures: A brief review. In: *Proceedings of the ISRM SINOROCK 2013*. Shanghai, China 18–20 June.
- Lasseux, D., Abbasian Arani, A.A., Ahmadi, A., 2011. On the stationary macroscopic inertial effects for one phase flow in ordered and disordered porous media. *Phys. Fluids* 23, 073103 (2011).
- Magnin, P.J., Piau, J.M., 2004. Viscoplastic fluid flow through a sudden axisymmetric expansion. *AIChE J.* 47 (10), 2155–2166.
- Malvalut, G., Ahmadi, A., Omari, A., 2017. Numerical simulation of yield stress fluid flow in capillary bundles: influence of the form and the axial variation in the cross section. *Transp. Porous Media* 120, 255–270.
- Mehmani, Y., Tchepeli, H., 2016. Pore-network modeling vs. direct numerical simulation: a comparative study. *Proceedings of the AGU Fall Meeting Abstracts*.
- Mehmani, Y., Tchepeli, H.A., 2017a. Minimum requirements for predictive pore-network modelling of solute transport in micromodels. *Adv. Water Res.* 108, 83–98.
- Mehmani, Y., Tchepeli H., 2017b. PNM vs. DNS Intercomparison Dataset for Transport in Micromodels. Digital Rocks Portal. Retrieved March 28, from [www.digitalrockportal.org](http://www.digitalrockportal.org).

- Moreno, E., Larese, A., Cervera, M., 2016. Modelling of Bingham and Herschel–Bulkley flows with mixed P1/P1 finite elements stabilized with orthogonal subgrid scale. *J. Non Newtonian Fluid Mech.* 228, 1–16.
- Paul, S., Roy, S., Ghosh, P., Faghihi Zarandi, M.A., Cender, T., Pillai, K.M., 2019. A novel method for permeability estimation from micro-tomographic images. *Transp. Porous Media* 127, 127–171.
- Pawlowski, S., Nayak, N., Meireles, M., Portugal, C.A.M., Velizarov, S., Crespo, J.G., 2018. CFD modelling of flow patterns, tortuosity and residence time distribution in monolithic porous columns reconstructed from X-ray tomography data. *Chem. Eng. J.* 350, 757–766.
- Perrin, C.L., Tardy, P.M.J., Sorbie, K.S., Crawshaw, J.C., 2006. Experimental and modeling study of Newtonian and non-Newtonian fluid flow in pore network micro-models. *J. Colloid Interface Sci.* 295, 542–550.
- Prashant, J.J. Derksen, Direct simulations of spherical particle motion in Bingham liquids, *Comput. Chem. Eng.* 2011;35(7): 1200–1214.
- Rodríguez de Castro, A., Agnaou, A., 2019. Numerical Investigation of the Apparent Viscosity Dependence on Darcy Velocity During the Flow of Shear-Thinning Fluids in Porous Media. *Transp. Porous Media* 129, 93–120.
- Rodríguez de Castro, A., Agnaou, M., Ahmadi-Sénichault, A., Omari, A., 2020. Numerical porosimetry: Evaluation and comparison of Yield Stress fluids Method, Mercury Intrusion Porosimetry and pore Network Modelling approaches. *Comput. Chem. Eng.* 133, 106662.
- Rodríguez de Castro, A., Ahmadi-Sénichault, A., Omari, A., Savin, S., Madariaga, L.-F., 2016. Characterizing porous media with the Yield Stress Fluids porosimetry Method. *Transp. Porous Media* 114 (1), 213–233.
- Rodríguez de Castro, A., Ahmadi-Sénichault, A., Omari, A., 2018. Using xanthan gum solutions to characterize porous media with the yield stress fluid porosimetry method: robustness of the method and effects of polymer concentration. *Transp. Porous Media* 122 (2), 357–374.
- Rodríguez de Castro, A., Omari, A., Ahmadi-Sénichault, A., Bruneau, D., 2014. Toward a New method of Porosimetry: Principles and Experiments. *Transp. Porous Media* 101 (3), 349–364.
- Sahimi, M., 1993. Nonlinear transport processes in disordered media. *AIChE J.* 39, 369–386.
- Saramito, P., Wachs, A., 2017. Progress in numerical simulation of yield stress fluid flows. *Rheol. Acta* 56, 211–230.
- Sivanesapillai, R., Steeb, H., Hartmaier, A., 2014. Transition of effective hydraulic properties from low to high Reynolds number flow in porous media. *Geophys. Res. Lett.* 41, 4920–4928. doi:10.1002/2014GL060232.
- Skelland, A.H.P., 1967. *Non-Newtonian Flow and Heat Transfer*. Wiley, New York.
- Sochi, T., Blunt, M.J., 2008. Pore-scale network modeling of Ellis and Herschel–Bulkley fluids. *J. Pet. Sci. Eng.* 60, 105–124.
- Spelt, P.D.M., Yeow, A.Y., Lawrence, C.J., Selerland, T., 2005. Creeping flows of Bingham fluids through arrays of aligned cylinders. *J. Non Newtonian Fluid Mech.* 129, 66–74.
- Talon, L., Bauer, D., 2013. On the determination of a generalized Darcy equation for yield-stress fluid in porous media using a lattice-Boltzmann TRT scheme. *Eur. Phys. J. E* 36, 139 (2013).
- Tsakiroglou, C.D., 2002. A methodology for the derivation of non-Darcian models for the flow of generalized Newtonian fluids in porous media. *J. Non Newtonian Fluid Mech.* 105, 79–110.
- Valdés-Parada, F.J., Porter, M.L., Wood, B.D., 2011. The Role of Tortuosity in Upscaling. *Transp. Porous Media* 88 (1), 1–30.
- Vidal, D., Ridgway, C., Pianet, G., Schoelkopf, J., Roy, R., Bertrand, F., 2009. Effect of particle size distribution and packing compression on fluid permeability as predicted by lattice-Boltzmann simulations. *Comput. Chem. Eng.* 33, 256–266.
- Xiong, Q., Baychev, T.G., Jivkov, A.P., 2016. Review of pore network modelling of porous media: Experimental characterisations, network constructions and applications to reactive transport. *J. Contam. Hydrol.* 192, 101–117.
- Zhang, M., Prodanovic, M., Mirabolghasemi, M., Zhao, J., 2019. 3D microscale flow simulation of shear-thinning fluids in a rough fracture. *Transp. Porous Media* 128, 243–269.
- Zhao, J., Kang, Q., Yao, J., Viswanathan, H., Pawar, R., Zhang, L., Sun, H., 2018. The effect of wettability heterogeneity on relative permeability of two-phase flow in porous media: a lattice Boltzmann study. *Water Resour. Res.* 54 (2), 1295–1311.